Physics-Informed Neural Network for Solving Hydrodynamic Lubrication Characteristics of Piston Pump Slipper Pair

Hanyu Gao[1], Hua Fang[1], Hao Liu[1*], Yan Tong[2], Dayong Yang[2], Xiaoping Ouyang[1*]

[1]State key laboratory of fluid power components and mechatronic systems, Zhejiang University Hangzhou, Zhejiang, China
[2]Shanghai Aircraft Manufacturing Co., Ltd. Shanghai, China
E-mail: henrygao@zju.edu.cn, fhua@zju.edu.cn, haoliu7850052@zju.edu.cn, tongyan@comac.cc, yangdayong@comac.cc, ouyangxp@zju.edu.cn

Abstract

The slipper pair is one of the key friction pairs, and its lubrication characteristics are one of the main difficulties in the study of aviation piston pumps. Traditional numerical models used to simulate the lubrication characteristics of friction pairs have problems such as slow calculation speed and poor convergence. Recently, the emergence of Physics-Informed Neural Networks has provided a new way to improve the simulation and solution of lubrication characteristics. Compared with traditional numerical models based on fluid dynamic lubrication theory, PINN provides a more efficient and flexible solution by embedding deep learning models into solving partial differential equations (PDEs). This paper proposes, for the first time, to integrate the prior knowledge of hydrodynamic lubrication in the friction pairs into neural networks, presenting a PINN-based model for solving the oil film characteristics of friction pairs, along with a corresponding training strategy. Simulation results on the slipper pair show that the PINN method effectively overcomes the limitations of traditional numerical methods, and can accurately predict lubrication characteristics and significantly shorten the computation time. The potential of PINN in modeling and solving lubrication characteristics is of great significance for the study and optimization of the friction pair characteristics in piston pumps.

Keywords: Piston pump; PINN; slipper; friction pair; lubrication; oil film

1 Introduction

Axial piston pumps, recognized for their high power density, output pressure, and efficiency, are widely utilized in aircraft hydraulic systems. The enhancement of aircraft flight performance and the need for weight reduction drive the ongoing improvement of power density in hydraulic systems and aviation piston pumps[1]. Increasing pressure and speed are effective ways to enhance the power density of aviation piston pumps[2,3]. The performance and longevity of aviation piston pumps are primarily influenced by three essential friction pairs: the slipper pair, the piston pair, and the port plate pair. The slipper pair, a vital component that connects the piston and the swash plate, plays a key role in maintaining the stability of the piston's reciprocating and linear composite movements, which enables the pump's oil suction and discharge functions. Optimal oil film characteristics are crucial for the reliable, long-term operation of the slipper pair. However, increases in pressure and speed can cause various issues in the slipper pair's oil film, including insufficient load-bearing capacity, unstable dynamics, lubrication failure, and increased temperature rise—all of which compromise the reliability and service life of the aviation piston pump. Thus, enhancing the oil film characteristics of the slipper pair is a critical strategy for improving the reliability and longevity of aviation piston pumps under high-pressure and high-speed conditions.

The characteristics of the slipper pair's oil film are influenced by the complex interaction of several factors, including materials, design, manufacturing, operating conditions, and environmental influences, with many of these elements mutually constraining each other. Consequently, it is impractical to rely solely on expert experience to optimize the oil film characteristics of the slipper pair, making high-precision modeling and simulation an essential process. Furthermore, modeling and simulation play a crucial role in uncovering formation mechanisms, analyzing evolution patterns, and monitoring or predicting the performance of the slipper pair's oil film.

At present, the modeling and simulation of the oil film in slipper pairs face three primary challenges. The primary challenge is the high-precision modeling difficulty caused by model complexity. Current modeling techniques are largely rooted in fluid lubrication theory and involve complicated interdependencies among various factors such as materials, design, manufacturing, operational conditions, and environmental aspects, as well as multiple physical domains like fluid dynamics, thermal fields, and solid mechanics. This complexity requires the simultaneous analysis of numerous physical equations, parameters, and constraints, making high-precision modeling difficult. The second challenge is the significant computational load associated with resolving complex partial differential equations. Existing models depend largely on numerical techniques, where the requirement for fine mesh discretization and strict iteration tolerance management makes it difficult to balance accuracy and efficiency. As a result, simulating the oil film of the slipper pair requires considerable computational time. The third challenge arises from the limited generalizability of customized models. Simulation models created for specific piston pump slippers are typically designed for particular structures and operating conditions, which makes them poorly equipped to handle wide variations in operating parameters or design changes. In practical engineering research and application, these restrictions notably impede the optimization efficiency of the slipper pair's oil film characteristics, slowing down the rapid iterative development of aviation piston pumps. Fortunately, the recent introduction of Physics-Informed Neural Networks presents a promising opportunity to tackle these challenges.

Physics-informed Neural Networks are models that incorporate existing knowledge of physical equations by embedding partial differential equations (PDEs) and boundary conditions (BCs) as constraints in the training process. This approach ensures the neural network is aligned with the defined physical principles during training constraints[4,5]. PINN provides a variety of benefits. To begin with, it can seamlessly integrate the governing equations of physical fields directly into the neural network, eliminating the requirement for intricate discrete solution frameworks. This greatly streamlines the process of solving PDEs and makes modeling easier. Once trained, PINN can also deliver solutions throughout the entire domain, bypassing the extensive grid calculations and iterative steps common in traditional numerical methods. As a result, it achieves high-accuracy solutions while significantly lowering computational demands time[6,7]. Moreover, the prediction and solution processes of a trained PINN model are exceptionally fast, avoiding the repeated iterations necessary in numerical computations and reducing computational burdens. Additionally, PINN is adaptable to various physical domains, as the training direction and rules can be easily modified by adjusting the loss function. Once trained, PINN models can be applied to similar problems for solutions, eliminating the need for re-modeling, grid discretization, and iterative calculations, thereby enhancing the generalizability of the solution process.

Currently, PINN is being extensively applied in various modeling and simulation fields, including fluid dynamics[8–10], mechanical modeling[11,12], and thermal characteristic modeling[13–15]. In the area of fluid lubrication, PINN has also shown significant promise. Initial advancements have been made in utilizing PINN to address lubrication-related characteristics in bearings. For instance, Almqvist[16] developed a physics-informed neural network to address initial and boundary value problems for solving one-dimensional Reynolds equations. Li et al. [17] introduced a ReF-nets model for determining the lubrication characteristics of gas bearings. Rom [18] employed PINN to solve two-dimensional Reynolds equations incorporating JFO cavitation modeling. Zhao et al. [19] compared the accuracy of FEM and PINN methods in solving two-dimensional Reynolds equations and analyzed the impact of different network layers and neuron counts on computational precision. Xi et al. [20] utilized PINN to address inverse problems in hydrodynamic lubrication for predicting journal-bearing parameters. These studies collectively underscore the immense potential of PINN in modeling and simulating fluid lubrication. In aviation piston pumps, the structure and state of the oil film in friction pairs are more complex than those in bearing oil films, featuring a more significant number of parameters and constraints, which poses greater challenges for PINN-based solutions. To date, no applications have been reported regarding the application of PINN in the oil film lubrication characteristics of slipper pair of aviation piston pump.

This study pioneers the application of the Physics-Informed Neural Network to the modeling of the oil film in the slipper pair of aviation piston pumps. By substituting the traditional two-dimensional Reynolds equation, typically used in numerical models for pressure distribution calculations, with a PINN-based approach, we greatly improve computational efficiency while preserving model accuracy. The subsequent sections of this paper are organized as follows: Section 2 introduces the numerical solution model for the slipper pair’s oil film. Section 3 details the development of the PINN-based oil film model and discusses the training strategies employed. Finally, Section 4 analyzes the performance of PINN in solving pressure distributions and compares the errors between PINN and numerical solutions under various parameters.

2 Slipper Pair Hydrodynamic Lubrication Model

2.1 Slipper Pair Overview

As a type of volumetric hydraulic pump, the axial piston pump primarily generates pressure and outputs high-pressure oil by altering its volume. Figure 1 illustrates a structure diagram of an aviation axial piston pump. The basic working principle is that rotational motion drives the piston to reciprocate within the cylinder bore, resulting in periodic changes in the volume of the piston chamber, which generates low suction pressure and high discharge pressure.

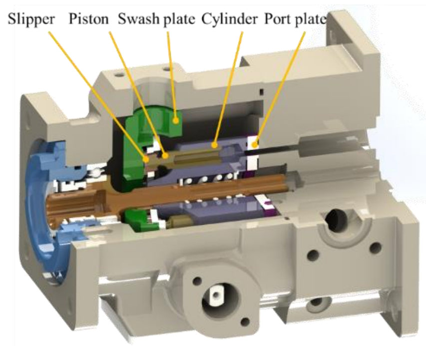

Figure 1: Aviation axial piston pump structure.

The slipper pair, which includes the slipper and the swash plate, forms a plane pair and serves as the primary force-transmitting component in an axial piston pump. Figure 2 illustrates the structure of the slipper pair. The design of the slipper pair is based on the principle of hydrostatic oil film support. High-pressure oil is introduced from the piston chamber into the oil pocket within the slipper pair, creating an oil film on the sealing band of the slipper. During actual operation, the slipper experiences a tilting moment that causes it to tilt at a certain angle. Consequently, the oil film in the slipper pair takes on a wedge-shaped profile, and the shape of this wedge-shaped oil film changes with variations in the slipper's tilting posture.

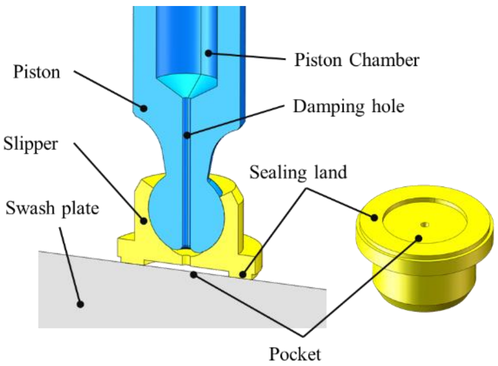

Figure 2: Slipper pair structure.

2.2 Mathematical Model

Firstly, according to the corresponding fluid mechanics assumptions and the continuity equation and NS equation, the two-dimensional Reynolds equation of the oil film of the sliding shoe pair in the polar coordinate system [21] is

$$\frac{1}{r}\frac{\partial}{\partial r}\left(r\frac{h^3}{\mu}\frac{\partial p}{\partial r}\right)+\frac{1}{r^2}\frac{\partial}{\partial \theta}\left(\frac{h^3}{\mu}\frac{\partial p}{\partial \theta}\right)=6\left(v_r\frac{\partial h}{\partial r}+v_\theta\frac{\partial h}{\partial \theta}\right) \tag{1}$$

where r is the radial distance, θ is the polar angle, h is the oil film thickness, μ is the viscosity, and v_r and v_θ are the radial and tangential velocities, respectively.

Since the oil film of the slipper pair is wedge-shaped, it is essential to derive the equation for oil film thickness based on the three-point coplanar geometric relationship. As illustrated in Figure 3, points A_1, A_2, and A_3 represent three locations on the outer edge of the slipper oil film with a phase difference of 120°, and the corresponding oil film thicknesses are h_1, h_2, and h_3, respectively. Therefore, the oil film thickness at any point on the bottom surface of the slipper, $h(r,\ \theta)$, can be expressed as:

$$h(r,\ \theta)=\frac{r\cos\theta}{3R}(2h_1-h_2-h_3)+\frac{r\sin\theta}{\sqrt{3}R}(h_2-h_3)+\frac{1}{3}(h_1+h_2+h_3) \tag{2}$$

Where R is the outer radius of the slipper sealing band:

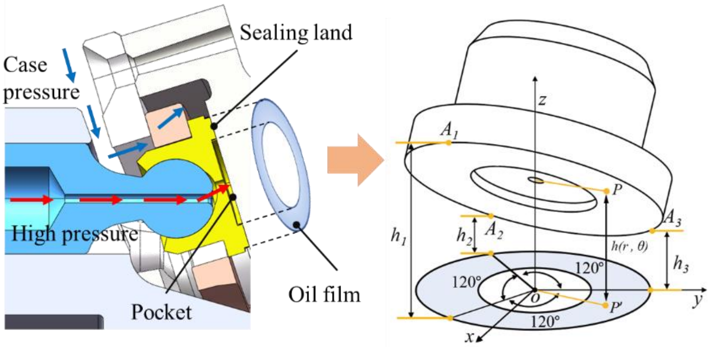

Figure 3: Oil film thickness model of slipper pair.

To reduce computational complexity and avoid instability in numerical calculations, the mathematical model undergoes dimensionless preprocessing. The introduction of dimensionless preprocessing provides a unified benchmark for comparison and eliminates the influence of physical parameters with different orders of magnitude on the subsequent PINN training [22], and helps prevent the imbalance of gradient size during the backpropagation process, thereby enhancing the stability of the training convergence. The equations for oil film pressure and thickness after dimensionless preprocessing are

$$\frac{1}{\bar{r}}\frac{\partial}{\partial \bar{r}}\left(\bar{r}H^3\frac{\partial P}{\partial \bar{r}}\right)+\frac{1}{\bar{r}^2}\frac{\partial}{\partial \theta}\left(H^3\frac{\partial P}{\partial \theta}\right)=6\left(V_r\frac{\partial H}{\partial \bar{r}}+V_\theta\frac{\partial H}{\partial \theta}\right) \tag{3}$$

$$H(\bar{r},\ \theta)=\frac{\bar{r}\cos\theta}{3R}(2H_1-H_2-H_3)+\frac{\bar{r}\sin\theta}{\sqrt{3}R}(H_2-H_3)+\frac{1}{3}(H_1+H_2+H_3) \tag{4}$$

where: the dimensionless oil film pressure is $P=p/p_0$, the dimensionless thickness is $H=h/h_0$, the dimensionless radial distance is $\bar{r}=r/R$, the dimensionless velocities are $V_r=v_r/v_{r0}$ and $V_\theta=v_\theta/v_{\theta 0}$ and the polar angle θ is inherently dimensionless. Assuming that viscosity is constant, the dimensionless viscosity can be regarded as 1.

Meanwhile, the partial derivative of the oil film thickness can also be derived as:

$$\begin{aligned}\frac{\partial H}{\partial \bar{r}}&=\frac{\sin\theta}{\sqrt{3}R}(H_2-H_3)+\frac{\cos\theta}{3R}(2H_1-H_2-H_3)\\ \frac{\partial H}{\partial \theta}&=\frac{\bar{r}\cos\theta}{\sqrt{3}R}(H_2-H_3)-\frac{\bar{r}\sin\theta}{3R}(2H_1-H_2-H_3)\end{aligned} \tag{5}$$

The Dirichlet boundary condition for solving the Reynolds equation is:

$$p(r_0,\ \theta)=p_{in}=1,\quad p(R,\ \theta)=p_{out}=0 \tag{6}$$

Given that the solution region is annular, the following additional periodic boundary conditions must be specified

$$p(r,\ 0)=p(r,\ 2\pi),\quad \left.\frac{\partial p}{\partial \theta}\right|_{(r,\ 0)}=\left.\frac{\partial p}{\partial \theta}\right|_{(r,\ 2\pi)} \tag{7}$$

2.3 Numerical Method

The oil film pressure equation governing the slipper pair is a standard elliptical partial differential equation with no analytical solution. This paper employs the finite volume method to derive the numerical solution. The oil film region for the slipper pair is discretized using polar coordinates, with the discrete grid representation is illustrated in Figure 4. For each discretized area, the volume integral is converted into a surface integral and simplified to the following equation

$$\int_w^e \int_s^n \frac{1}{\bar r}\frac{\partial}{\partial \bar r}\left(\bar r H^3 \frac{\partial P}{\partial \bar r}\right)\bar r d\bar r d\theta + \int_s^n \int_w^e \frac{1}{\bar r^2}\frac{\partial}{\partial \theta}\left(H^3 \frac{\partial p}{\partial \theta}\right)\bar r d\bar r d \\ = \oint 6\left(V_r \frac{\partial H}{\partial \bar r} + V_\theta \frac{\partial H}{\partial \theta}\right) \tag{8}$$

Eq. (8) is further discretized and organized into the form of linear equation.

$$a_p p_p = a_N p_N + a_S p_S + a_W p_W + a_E p_E + S \\ a_p = a_N + a_S + a_W + a_E \tag{9}$$

where:

$$a_{\mathrm{n}} = \bar r_{\mathrm{n}} (H^3)_{\mathrm{n}} \frac{\Delta\theta}{(\delta \bar r)_{\mathrm{n}}} \\ a_{\mathrm{s}} = \bar r_{\mathrm{s}} (H^3)_{s} \frac{\Delta\theta}{(\delta \bar r)_{\mathrm{s}}} \\ a_{\mathrm{e}} = \frac{1}{\bar r_{\mathrm{e}}} (H^3)_{\mathrm{e}} \frac{\Delta \bar r}{(\delta \bar r)_{\mathrm{e}}} \\ a_w = \frac{1}{\bar r_w} (H^3)_w \frac{\Delta \bar r}{(\delta \bar r)_w} \\ S = 6\left(V_r \frac{\partial H}{\partial \bar r} + V_\theta \frac{\partial H}{\partial \theta}\right) \bar r_{\mathrm{p}} \Delta\theta \Delta\bar r \tag{10}$$

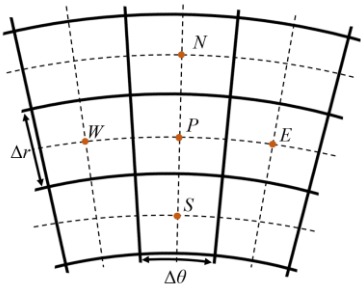

Figure 4: Oil film pressure discrete grid.

The Gauss-Seidel over-relaxation iterative method is employed to solve the discretized equation of the oil film pressure field, and the iterative format of the pressure calculation can be expressed as

$$P_p^{k+1} = \alpha\left(\frac{a_n P_n^k + a_s P_s^{k-1} + a_e P_e^k + a_w P_W^{k-1} + S}{a_p} - P_p^k\right) + P_p^k \tag{11}$$

where α is the over-relaxation coefficient, P_p^k is the pressure at the current iteration, P_p^{k-1} is the pressure from the previous iteration, and P_p^{k+1} is the pressure for the next iteration.

In the process of numerical iteration, the convergence residual is defined as:

$$\left|\frac{p_{\mathrm{p}}^{(k)} - p_{\mathrm{p}}^{(k-1)}}{p_{\mathrm{p}}^{(k)}}\right| \leqslant err \tag{12}$$

When the convergence residual error is below the threshold of 10^{-8}, the current computation is regarded as converged. The pressure values calculated for all nodes together create the pressure field distribution on the bottom surface of the slipper.

The overall flow chart of the numerical solution is illustrated in Figure 5.

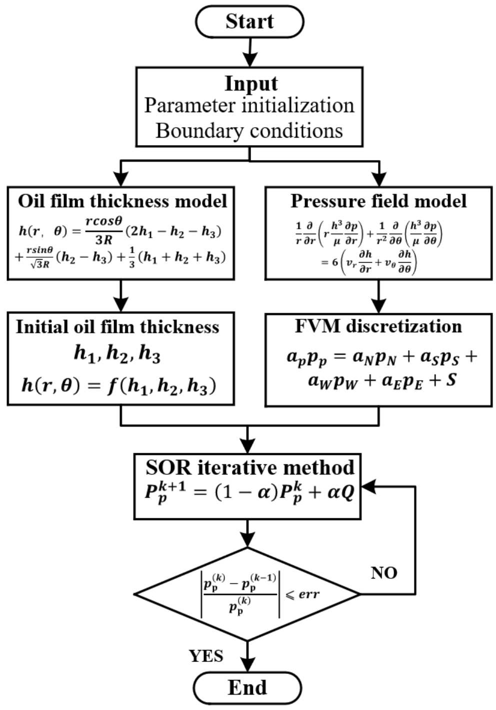

Figure 5: *Flow chart for the numerical solution of oil film pressure.*

3 PINN method

Figure 6 shows a PINN model designed to address the oil film problem in the slipper pair. The PINN model consists of two main components: the neural network block on the left and the physical information constraint block on the right. We chose a standard Artificial Neural Network model (ANN) for the neural network. The inputs to the neural network are the coordinates (r, θ) of the solution domain, and the output is an approximation or prediction of the Reynolds equation solution $P(r, \theta)$.

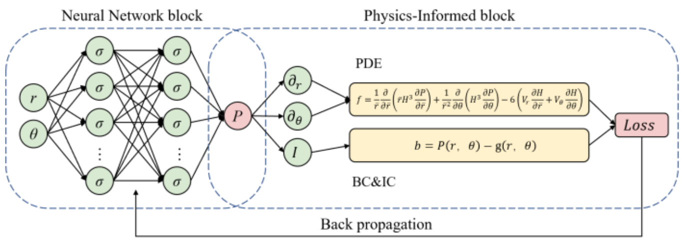

Figure 6: *The PINN Framework for Oil Film Pressure of Slipper Pair*

The objective of training the PINN is to minimize the residuals, which include both boundary condition residuals and PDE residuals. During the training process, the neural network samples across the entire solution domain to generate predicted pressure values for each sampling point. A total of Nb training points are selected on the inner and outer boundaries of the domain (represented by red dots in Figure 7), while Nf sampling points are gathered within the domain (represented by blue dots in Figure 7). The predicted pressure values at these sampling points are utilized to compute derivatives with respect to the inputs r and θ through automatic differentiation (AD) enabled by the neural network. These results are then input into the physics-informed constraint block to calculate the boundary condition residuals and PDE residuals, which are combined into the loss function. Through iterative training via backpropagation, the loss value is minimized, ultimately leading to the optimal solution and concluding the PINN training process.

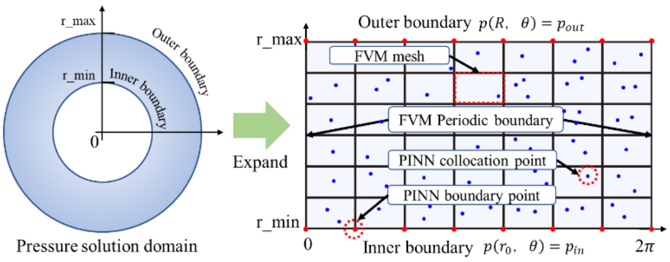

Figure 7: Solution domain and boundary conditions of slipper pair oil film.

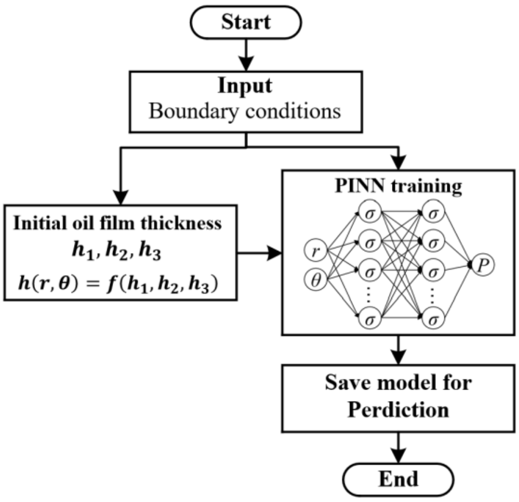

Figure 8: *Flow chart for the PINN-based solution of oil film pressure.*

3.1 Loss function

The loss function determines the training direction of PINN. In this paper, the total loss function $Loss_{mse}$ of the PINN model is the sum of the residuals and PDE residuals of all training points on the inner and outer boundaries, as shown in Formula (14). In each iterative training, the weight and bias parameters of ANN are updated by using iterative optimization algorithms such as Adam or SGD to minimize the total loss $Loss_{mse}$.

The weight coefficient chosen for the loss function heavily affects the optimization direction and effectiveness of the PINN. A loss term with a high weight coefficient indicates it has a substantial impact on the overall loss, thus influencing its optimization during the iterative training phases. Therefore, it is essential to establish an appropriate balance between the weight coefficients of the loss function. In formula (14), we set the weight values of the loss function as β_1=100， β_2=10， and β_3=10, respectively.

$$\begin{cases} loss1 = \frac{1}{Nf}\sum_{i=1}^{Nf}\left\| \frac{1}{\bar{r}}\frac{\partial}{\partial \bar{r}}\left(\bar{r}H^3\frac{\partial P}{\partial \bar{r}}\right) + \frac{1}{\bar{r}^2}\frac{\partial}{\partial \theta}\left(H^3\frac{\partial P}{\partial \theta}\right) - 6\left(V_r\frac{\partial H}{\partial \bar{r}} + V_\theta\frac{\partial H}{\partial \theta}\right)\right\|^2 \\ loss2 = \frac{1}{Nb}\sum_{i=1}^{Nb}\|\hat{p} - p_{in}\|^2 \\ loss3 = \frac{1}{Nb}\sum_{i=1}^{Nb}\|\hat{p} - p_{out}\|^2 \end{cases} \tag{13}$$

$$Loss_{mse} = \beta_1 loss1 + \beta_2 loss2 + \beta_3 loss3 \tag{14}$$

3.2 Network structure and activation function

Choosing hyperparameters for neural networks is a task that significantly depends on empirical knowledge, as their suitability directly affects the model's convergence, accuracy, and computational efficiency. Based on previous research on Physics-Informed Neural Networks, the PINN model in this study utilizes a 6-layer neural network architecture, which comprises four hidden layers with 50 neurons in each layer.

In Physics-Informed Neural Networks, the commonly used ReLU (Rectified Linear Unit) function is not suitable for scenarios that require higher-order derivative calculations due to its non-differentiability at zero. Relevant studies [17] have compared the computational performance of the sigmoid, hyperbolic tangent (tanh), and cosine functions as activation functions, showing that the hyperbolic tangent function demonstrates superior performance in terms of iteration speed and computational accuracy. Therefore, this study selects the hyperbolic tangent function as the nonlinear activation function.

3.3 Weight initialization strategy

In training neural networks, weight initialization significantly affects the network's convergence speed and training efficiency. Commonly used initialization methods include Glorot (Xavier) initialization and He initialization, among others. The choice of initialization method closely relates to the activation function. To ensure compatibility with the hyperbolic tangent activation function, this study uses Glorot uniform initialization to set the neural network's weights.

The core idea of Glorot initialization [23] is to adjust the range of initial weights based on the input and output dimensions to avoid the problems of vanishing or exploding gradients. In Glorot initialization, each weight element is randomly drawn from a uniform distribution within the range [-a, a], where a is determined by the number of neurons in the input layer n_{in} and the number of neurons in the output layer n_{out}. The range of possible weight values can be determined as:

$$\text{Weight} \sim \text{Uniform}\left(-\sqrt{\frac{6}{n_{\text{in}} + n_{\text{out}}}}, \sqrt{\frac{6}{n_{\text{in}} + n_{\text{out}}}}\right) \tag{15}$$

3.4 Optimizer

The choice of optimizer significantly impacts the training efficiency and accuracy of Physics-Informed Neural Networks (PINNs). The loss function of PINNs is often complex, encompassing the residuals of physical equations as well as boundary condition constraints. This paper adopts a combined optimization strategy. In the early stages of training, when the residuals exhibit significant fluctuations, the Adam optimizer is utilized to manage the highly nonlinear loss function, accelerating the convergence process by adaptively adjusting the learning rate. Once the residual loss stabilizes and the decline becomes gradual, the optimization shifts to the second-order L-BFGS optimizer to fine-tune the update direction and step size for each parameter, further enhancing the accuracy of the results. The L-BFGS optimizer greatly improves the precision of the solution during the later stages of PINN training, meeting the high-accuracy requirements for solving partial differential equations (PDEs). Although its computational cost is relatively high, it remains completely acceptable given the scale of the training task in this study.

Additionally, 10,000 sample points are established in the solution domain, and 400 sample points are placed on the boundary to ensure the adequacy of the training data and accurately meet the boundary conditions.

4 Results And Discussion

In the preceding sections, we introduced the Physics-Informed Neural Network model for solving the Reynolds equation that governs the lubrication of the slipper pair, encompassing the model's principles and detailed configurations. In this section, we validate the model's performance and analyze the influence of various boundary parameters on its effectiveness.

4.1 Parameters and solution environment

This paper utilizes the same hardware and software setup for the numerical calculations and the implementation of the PINN. The environmental configuration details are as follows: the numerical computation is performed using Python 3.11.11, the deep learning framework is Pytorch 2.2.0 running on a Windows 10 system, and the hardware consists of an Nvidia 4090 with 24GB memory and an Intel i9-10900K processor at 3.7GHz.

The solution parameters for the numerical model and the PINN model are presented in Table 1. The parameters of the slipper pair, derived from both the numerical calculation and the PINN model, match the boundary conditions and are scaled identically using dimensionless methods.

Table 1: Parameter setting.

Parameter	Value	Unit
Radial grid number	30	
Angular grid number	120	
Error control	1e-8	
Piston pump rotational speed	12000	rpm
Outer radius of the slipper pair sealing band	3.85	mm
Inner radius of the slipper pair sealing band	2.5	mm
Oil film thickness of the characteristic point （vanilla）	10，12，8	μm
Number of pistons/slippers	9	
Piston pump swashplate angle	17	°
Oil viscosity	0.046	Pa*s

4.2 Model performance

The results of the model are illustrated in Figure 9, where (a), (b), and (c) represent the numerical solution results of the pressure distribution, the PINN solution results, and the absolute value error between the PINN and numerical solutions, respectively. The vertical axis of the figure indicates the dimensionless pressure value, while the horizontal axis corresponds to the dimensionless Cartesian coordinate. (d) shows the oil film thickness distribution. The vertical axis in this section refers to the dimensionless oil film thickness value, and the horizontal axis corresponds to the dimensionless Cartesian coordinate, consistent with the pressure distribution. (e) depicts the change in the loss curve of the PINN model during the training process. Initially, the loss value is high, and the Adam optimizer is employed. The loss value decreases rapidly with oscillation. After 8000 training steps, it drops to the specified accuracy and transitions to a second-order optimizer for smooth fine-tuning. After approximately 12000 training steps, the loss value stabilizes and remains unchanged, which may be regarded as convergence.

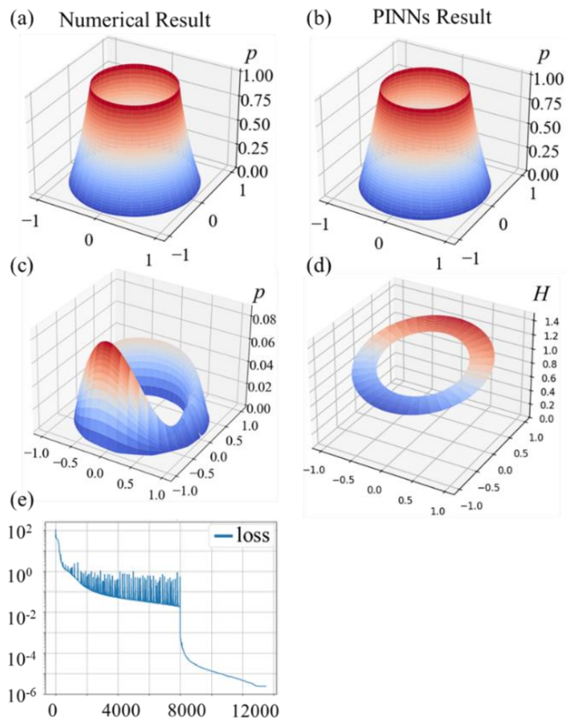

Figure 9: Oil film pressure solution results. (a) Numerical Method Result (b) PINN Method Result (c) Error between PINN and Numerical Solution (d) Oil Film Thickness Distribution (e)PINN Training Loss.

Because the central hole of the slipper is connected to the high-pressure oil in the plunger cavity, and the outer edge pressure of the slipper matches the case pressure, the oil film pressure distribution of the slipper pair exhibits high pressure in the central area that gradually decreases to low pressure at the edges. Figure 9 (a) and (b) illustrate that the results from PINN are highly consistent with the numerical solutions, and the pressure distribution is uniform and continuous. Figure 9 (c) further shows that the solution error of PINNs is very low. A thorough quantitative error analysis follows, comparing several different error calculation methods, as presented in Table 2. The error remains low within the solution domain. Analyzing the shape of the error region reveals that larger deviations occur in two areas, correlating with the oil film thickness distribution shown in Figure 9 (d), which appears at both sides of the larger oil film overturning angle. The oil film is wedge-shaped, leading to an uneven thickness distribution, with overturning angles along both horizontal axes. This may be attributed to the PINN method's sensitivity to the oil film thickness angle, resulting in a non-uniform distribution of calculation errors.

Table 2: Error Comparison.

Error Type			
Relative Error	Mean Squared Error	Root Mean Squared Error	Mean Absolute Error
6.54E-02	1.21E-03	3.48E-02	2.86E-02

Table 3 displays the numerical solution time along with the average time utilized for PINN training and prediction. It can be seen that the training time of the PINNs method is longer than the simulation time of the numerical method. However, the more significant advantage of the PINN approach lies in its greatly reduced prediction or reasoning time. The prediction time of PINN shows an order of magnitude improvement compared to numerical calculation, being approximately 282 times faster. The trained model can be employed for prediction calculations by retaining the neural network's weight settings, eliminating the need for the iterative process of numerical calculations. Similar research also points out that[24], although the calculation cost of training neural network is high in the early stage, the prediction of pressure distribution after training is several orders of magnitude faster than that of numerical simulation, and the prediction time is relatively stable, which is not easily affected by grid density.

Table 3: Average Computation Durations.

Task	Time		
	Simulation	Training	Prediction
Numerical Method	10.454s	\	\
PINN method	\	240.945s	0.037s

4.3 Influence of oil film thickness

Additionally, we compare the solving performance of the PINN model using different parameters. With all other parameters held constant, we assess the model's effectiveness at various rotational speeds. First, we examine how changes in oil film thickness affect the solution, since oil film thickness is crucial in solving the Reynolds equation. Even slight adjustments in thickness can greatly impact the results of the solution.

We conducted a comparative analysis of solutions for three different oil film thicknesses, as shown in the first row of Figure 10, which presents three distinct oil film thickness distributions: a flat oil film and two wedge-shaped oil films with different tilt directions. The flat oil film represents an ideal state where the slipper and swash plate are perfectly parallel, resulting in a uniform oil film thickness. However, under practical operating conditions, factors such as load variations, installation errors, and mechanical vibrations introduce an inclination between the slipper and swash plate, leading to non-uniform oil film thickness. According to the Reynolds equation, oil film pressure increases as oil film thickness decreases. Consequently, the pressure gradient shows a correspondingly higher variation on the thinner side of the wedge-shaped oil film.

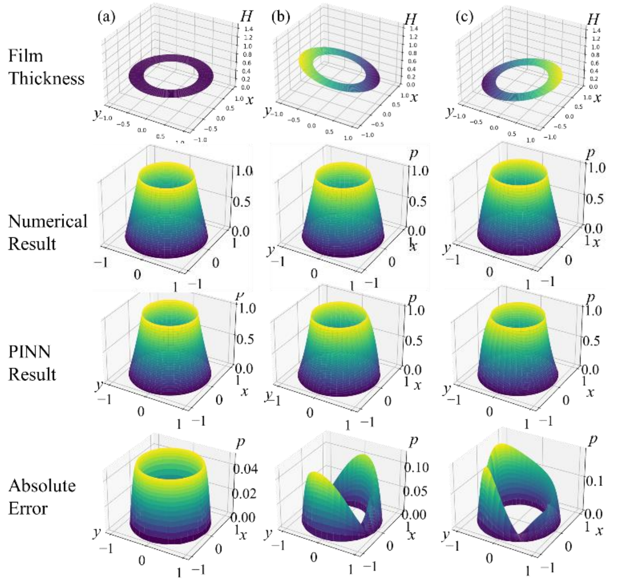

Figure 10: *Solution comparison under different oil film thicknesses.*

By comparing the three states of oil films, we can see that the results from the PINN solution closely align with those from numerical calculations. This indicates that PINN effectively captures how changes in oil film thickness influence pressure distribution. However, the distribution of oil film thickness significantly impacts the pressure distribution within the slipper pair. When the oil film is flat, the calculation error between the two methods is very small and nearly negligible. Under wedge-shaped lubricating film conditions, the pressure distribution demonstrates non-uniform characteristics, where error distribution predominantly manifest in areas with pronounced pressure gradient variations. Different error characteristics are illustrated in Figure 11. This discrepancy may stem from PINN's larger error in regions with a significant pressure gradient change. To enhance calculation accuracy across various oil film thickness distributions, it may be necessary to refine the sampling strategy during training and adjust the density of sampling points in accordance with oil film thickness.

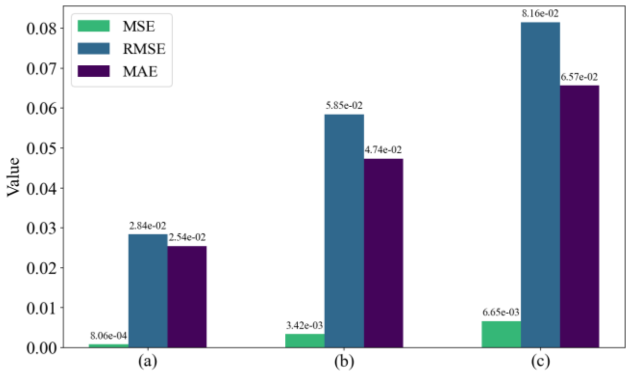

Figure 11: Comparison of pressure solution errors under different oil film thicknesses.

4.4 Influence of pressure boundary

Similarly, we utilized the data and oil film thickness distribution from the solution parameters for the numerical model and the PINN model are presented in Table 1. The parameters of the slipper pair, derived from both the numerical calculation and the PINN model, match the boundary conditions and are scaled identically using dimensionless methods. Figure 12 shows the results under different boundary pressures. The effect of varying the boundary pressure on the internal pressure distribution of the oil film is quite direct. The pressure distribution patterns obtained from the PINN model under different boundary pressures align with those derived from the numerical method. This demonstrates that the PINN model possesses strong generalization capabilities and can adapt to diverse boundary conditions.

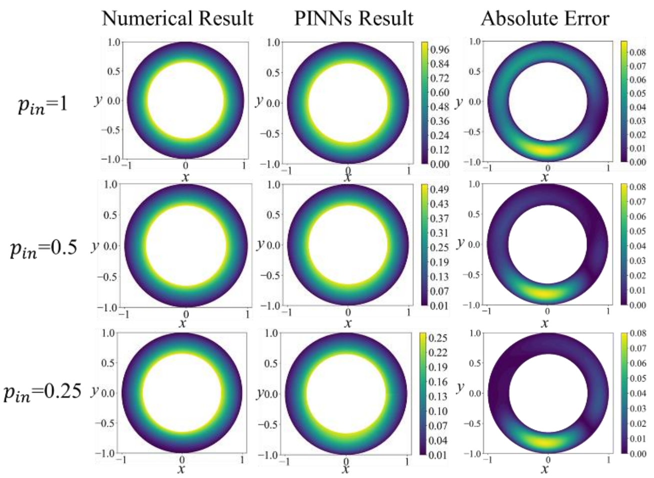

Figure 12: Solution comparison under different boundary pressures.

In the error distribution mode, similar to the previous analysis regarding the impact of oil film thickness, the error associated with smaller oil film thickness shows a larger peak. The error distribution is more confined near the pressure boundary, while the pressure gradient is greater in the middle layer. As the boundary pressure decreases, the absolute value of the error decreases slightly, and the distribution area also contracts. Different types of error pairs are illustrated in Figure 13.

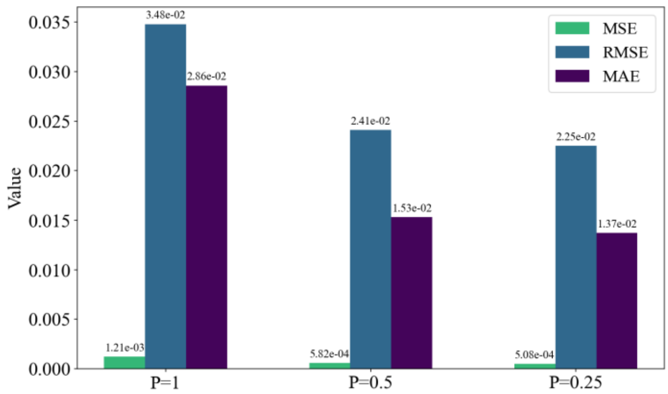

Figure 13:Comparison of pressure solution errors under different pressure boundaries.

4.5 Influence of rotational speed

We further assess the solution performance at various speeds, as shown in Figure 14, and evaluate the oil film distribution at 12000 rpm, 8000 rpm, and 4000 rpm. The error comparison is illustrated in Figure 15. Unlike the alterations made to the pressure boundary conditions, the change in rotational speed has a relatively minor effect on the error. From the error distribution across the three cases, as rotational speed increases, the overall error level rises slightly; however, the degree of change is noticeably smaller than that observed with the pressure boundary, indicating that PINN demonstrates greater stability when addressing the dynamic pressure effect.

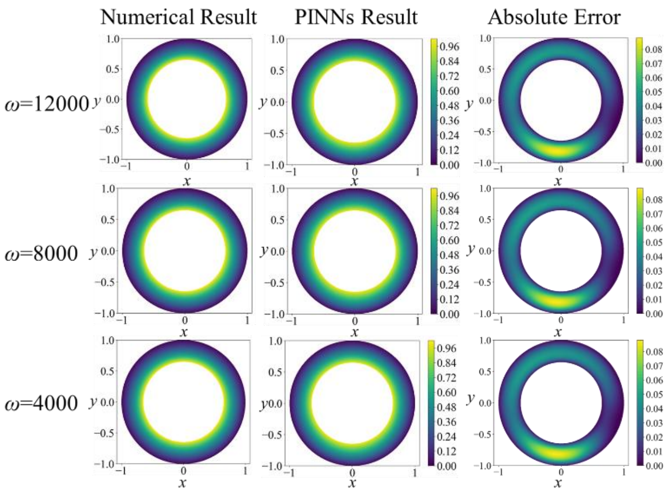

Figure 14: Solution comparison under different rotational speeds.

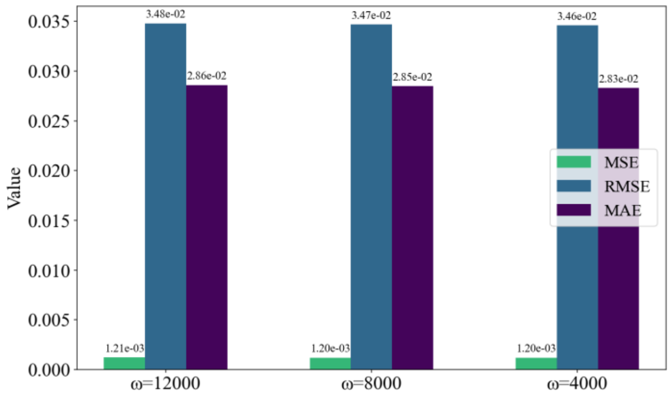

Figure 15: Comparison of pressure solution errors under different rotational speed conditions.

Although the aforementioned related discussions have proved the effectiveness and accuracy of PINN in solving the Reynolds equation of slipper pair, it must be admitted that it still faces challenges in the practical application of lubrication analysis. At present, PINN only solves the lubrication characteristics under specific parameters. Due to the complex motion and force of the slipper in actual operation, these constraints need to be added to the training of the model to improve the generalization of the model. However, more physical constraints are integrated into the loss function as soft penalty terms, which will lead to gradient imbalance between these constraints, and then lead to training failure or inaccurate enforcement of boundary conditions. Future work needs to further improve the structure or optimization strategy of PINN and extend the training model to complex working conditions including squeezing motion.

5 Conclusion

This study proposes a method utilizing PINN to analyze the lubrication characteristics of high-speed piston pump slippers, verifying the potential of PINN in addressing complex hydrodynamic lubrication issues. The results from comparisons with traditional numerical approaches indicate that PINN effectively handles complex nonlinear hydrodynamic lubrication equations, accurately capturing oil film pressure distribution and changes in film thickness during the lubrication of slipper pairs. Analyzing different operational parameters, including speed, boundary pressure, and oil film thickness, demonstrates that the PINN method demonstrates high solution accuracy, adaptability, and robustness. Nonetheless, PINN encounters challenges related to accuracy, convergence speed, and generalization in real-world applications, indicating a need for further optimization of the network structure and refinement of the training strategy to enhance performance, so that it has the potential to be extended to solve the problems including extrusion motion and elastic deformation. Overall, this paper presents an innovative deep-learning technique for modeling and calculating lubrication characteristics in piston pumps, which is anticipated to impact the design and optimization of high-speed piston pumps significantly.

Acknowledgment

This research was funded by the National Natural Science Foundation of China (Grant No. U2141209), the Aeronautical Science Foundation of China (Grant No. 20182876003 and 20240028076003), and the Natural Science Foundation of Zhejiang Province (Grant No. LQ23E050013).

Corresponding authors:

Hao Liu: haoliu7850052@zju.edu.cn;

Xiaoping Ouyang: ouyangxp@zju.edu.cn.

Nomenclature

Designation	Denotation	Unit
r	Polar radius	m
θ	Polar coordinate angle	rad
r_0	Radius of inner sealing belt of slipper	m
R	Radius of outer sealing belt of slipper	m
h	Slipper film thickness	μm
μ	Oil viscosity	Pa*S
v_r, v_θ	Slipper velocity	m/s
h_1, h_2, h_3	Oil film thickness of feature points	μm
P	Dimensionless oil film pressure	
H	Dimensionless oil film thickness	
$\bar{r}$	Dimensionless polar radius	
V_r, V_θ	Dimensionless velocity	
p_{out}	Pressure outer boundary conditions	
p_{in}	Pressure inner boundary condition	

References

[1] J Zhao, Y Fu, J Ma, J Fu, Q Chao, and Y Wang. Review of cylinder block/valve plate interface in axial piston pumps: Theoretical models, experimental investigations, and optimal design. *Chinese Journal of Aeronautics*, 34: (1) 111–134, 2021. https://doi.org/10.1016/j.cja.2020.09.030.

[2] B Zhang, C Zhao, H Hong, G Cheng, H Yang, S Feng, J Zhai, and W Xiao. Optimization of the outlet unloading structure to prevent gaseous cavitation in a high-pressure axial piston pump. *Proceedings of the Institution of Mechanical Engineers, Part C: Journal of Mechanical Engineering Science*, 236: (7) 3459–3473, 2022. https://doi.org/10.1177/09544062211043129.

[3] J Zhang, H Xu, J Chen, W Huang, X Huang, F Lyu, B Xu, M Pan, and Q Su. Modeling and Analysis of the tilt

behavior of the cylinder block in a high-speed axial piston pump. *Mechanism and Machine Theory*, 170: 104735, 2022. https://doi.org/10.1016/j.mechmachtheory.2022.104735.

[4] M Raissi, P Perdikaris, and G E Karniadakis. Physics-informed neural networks: A deep learning framework for solving forward and inverse problems involving nonlinear partial differential equations. *Journal of Computational Physics*, 378: 686–707, 2019. https://doi.org/10.1016/j.jcp.2018.10.045.

[5] G E Karniadakis, I G Kevrekidis, L Lu, P Perdikaris, S Wang, and L Yang. Physics-informed machine learning. *Nature Reviews Physics*, 3: (6) 422–440, 2021. https://doi.org/10.1038/s42254-021-00314-5.

[6] C Zhao, F Zhang, W Lou, X Wang, and J Yang. A comprehensive review of advances in physics-informed neural networks and their applications in complex fluid dynamics. *Physics of Fluids*, 36: (10) 101301, 2024. https://doi.org/10.1063/5.0226562.

[7] L Lu, X Meng, Z Mao, and G E Karniadakis. DeepXDE: A Deep Learning Library for Solving Differential Equations. *SIAM Review*, 63: (1) 208–228, 2021. https://doi.org/10.1137/19M1274067.

[8] Y Tian, M Woodward, M Stepanov, C Fryer, C Hyett, D Livescu, and M Chertkov. Lagrangian large eddy simulations via physics-informed machine learning. *Proceedings of the National Academy of Sciences*, 120: (34) e2213638120, 2023. https://doi.org/10.1073/pnas.2213638120.

[9] F Lorenzen, A Zargaran, and U Janoske. Potential of physics-informed neural networks for solving fluid flow problems with parametric boundary conditions. *Physics of Fluids*, 36: (3) 037143, 2024. https://doi.org/10.1063/5.0193952.

[10] Y Xiao, L M Yang, C Shu, H Dong, Y J Du, and Y X Song. Least-square finite difference-based physics-informed neural network for steady incompressible flows. *Computers & Mathematics with Applications*, 175: 33–48, 2024. https://doi.org/10.1016/j.camwa.2024.08.035.

[11] E Haghighat, M Raissi, A Moure, H Gomez, and R Juanes. A physics-informed deep learning framework for inversion and surrogate modeling in solid mechanics. *Computer Methods in Applied Mechanics and Engineering*, 379: 113741, 2021. https://doi.org/10.1016/j.cma.2021.113741.

[12] J Wang, Y L Mo, B Izzuddin, and C-W Kim. Exact Dirichlet boundary Physics-informed Neural Network EPINN for solid mechanics. *Computer Methods in Applied Mechanics and Engineering*, 414: 116184, 2023. https://doi.org/10.1016/j.cma.2023.116184.

[13] J Mai, Y Li, L Long, Y Huang, H Zhang, and Y You. Two-dimensional temperature field inversion of turbine blade based on physics-informed neural networks. *Physics of Fluids*, 36: (3) 037114, 2024. https://doi.org/10.1063/5.0190429.

[14] H Bararnia, and M Esmaeilpour. On the application of physics informed neural networks (PINN) to solve boundary layer thermal-fluid problems. *International Communications in Heat and Mass Transfer*, 132: 105890, 2022. https://doi.org/10.1016/j.icheatmasstransfer.2022.105890.

[15] T P Agatho, Pranowo, and A W R Emanuel. Solving the two-dimensional conduction heat transfer problem by using artificial neural network method, 2023 14th Int. Conf. Inf. Commun. Technol. Syst. ICTS, 2023: pp. 228–231. https://doi.org/10.1109/ICTS58770.2023.10330864.

[16] A Almqvist. Fundamentals of Physics-Informed Neural Networks Applied to Solve the Reynolds Boundary Value Problem. *Lubricants*, 9: (8) 82, 2021. https://doi.org/10.3390/lubricants9080082.

[17] L Li, Y Li, Q Du, T Liu, and Y Xie. ReF-nets: Physics-informed neural network for Reynolds equation of gas bearing. *Computer Methods in Applied Mechanics and Engineering*, 391: 114524, 2022. https://doi.org/10.1016/j.cma.2021.114524.

[18] M Rom. Physics-informed neural networks for the Reynolds equation with cavitation modeling. *Tribology International*, 179: 108141, 2023. https://doi.org/10.1016/j.triboint.2022.108141.

[19] Z Yang, L Guo, and P Wong. Application of physics-informed neural network in the analysis of hydrodynamic lubrication. *Friction*, 11: 2022. https://doi.org/10.1007/s40544-022-0658-x.

[20] Y Xi, and R Sun. Inverse problems in hydrodynamics lubrication: parameter identification in the reynold equation by using physics-informed neural networks. *Proceedings of the Institution of Mechanical Engineers, Part J: Journal of Engineering Tribology*, 13506501241291403, 2024. https://doi.org/10.1177/13506501241291403.

[21] A Schenk. Predicting lubrication performance between the slipper and swashplate in axial piston hydraulic machines. *Open Access Dissertations*, 2014. https://docs.lib.purdue.edu/open_access_dissertations/359.

[22] S Roy, D R Sarkar, C Annavarapu, P Roy, B Lecampion, and D M Valiveti. Adaptive interface-PINNs (AdaI-PINNs) for transient diffusion: applications to forward and inverse problems in heterogeneous media. *Finite Elements in Analysis and Design*, 244: 104305, 2025. https://doi.org/10.1016/j.finel.2024.104305.

[23] X Glorot, and Y Bengio. Understanding the difficulty of training deep feedforward neural networks, 2010. https://www.semanticscholar.org/paper/Understanding-the-difficulty-of-training-deep-Glorot-Bengio/b71ac1e9fb49420d13e084ac67254a0bbd40f83f.

[24] N Hess, and L Shang. Development of a Machine Learning Model for Elastohydrodynamic Pressure Prediction in Journal Bearings1. *Journal of Tribology*, 144: (8) 2022. https://doi.org/10.1115/1.4053815.